annalen der physik
www.ann-phys.org

Janus Device Based on Liquid Crystal Regulation with a Large Incidence Angle: Analogous Quantum Optical Effect and Absorption

Si-yuan Liao, Jun-yang Sui, Qi Chen, Hai-Feng Zhang, and Bing-Xiang Li**

In this paper, a Janus metastructure device (JMD) is proposed. The JMD design introduces asymmetric structures, which leads to the generation of analogous quantum optical effects when light is incident at large angles. Specifically, forward electromagnetic-induced transparency (EIT) and backward narrowband absorption (NA) are achieved when light is incident along different directions, displaying Janus characteristics in the forward and backward directions. Additionally, the operating frequency of JMD can be controlled through the use of liquid crystal. Such features hold promising potential for various applications in photonic and optoelectronic fields. When the axial direction of the liquid crystal is oriented along the *x*-direction, the JMD achieves a transparent window over 90% within 0.46–0.51 THz at forward incidence, and an absorption peak of 84.1% appears at 0.331 THz at backward incidence. When the axial direction is oriented along the *y*-direction, the JMD achieves EIT in the range of 0.51–0.575 THz at forward incidence, and a backward absorption peak of 93.3% occurs at 0.305 THz. In addition, the performance changes at different polarization and incidence angles are presented. The mechanism of absorption generation, the method of suppressing excess absorption, and the parametric inversion of the electromagnetic characteristics of JMD are also discussed.

1. Introduction

As an artificially manufactured periodic subwavelength structure, metastructure possesses many excellent properties that cannot be replaced by traditional materials, and can also show analogous quantum optical effects or interesting features, such as electromagnetic-induced transparency (EIT),[1,2] narrowband absorption (NA),[3,4] metalens,[5] and frequency selective surfaces.[6] Therefore, metastructure has gradually demonstrated unique advantages in functional integration and multifunctional control fields. Metastructures that integrate different functionalities in the forward and backward directions, inspired by Roman mythology, are called Janus metastructure devices (JMD), which has nonreciprocal characteristics in the forward and backward directions.[7,8] It is worth mentioning that in some cases, Janus properties are more significant at a large incidence angle, and such a phenomenon makes JMD devices well-suited for applications such as solar energy harvesting, signal processing, etc. For example, Zhang et al. used Janus hybrid materials to combine hydrophilic and solar energy harvesting for efficient solar desalination at large angular incidence.[9] Picardi et al. achieved the Janus dipole to further modulate the spin momentum through techniques such as the quantum spin-Hall effect.[10] McPolin et al. realized Janus dipolar sources that can be used in quantum technology through specific arrangements of nanostructures coupled to waveguide structures.[11]

To achieve multifunctional integration, a common method is to use external conditions, such as sonic wave,[12] light,[13] temperature,[14] pressure,[15] voltage,[16] etc., to change the physical properties of the material, thus achieving functional switching under different environmental conditions. In the field of electronic control, liquid crystal, as an emerging popular material, can be used to control the phase and polarization of electromagnetic waves due to its anisotropy. Anisotropic materials refer to materials whose physical or chemical properties exhibit spatial asymmetry, such as the refractive index of biaxial crystals showing anisotropy. Compared with other electronic control materials, liquid crystal has the characteristics of wide working bandwidth, low insertion loss, and stable electromagnetic properties.[17] In addition, due to its unique liquid characteristics, it has advantages that traditional electronic control materials do not possess.

One of the typical phenomena of the analogous quantum optical effects callled EIT was first observed in a three-level atomic system by Boyle et al. in 1991.[18] The characteristic of this phenomenon is the appearance of a sharp transmission window in the continuous reflection or absorption spectrum,[19] which has important applications in the fields of sensing,[20] signal processing,[21] slow light,[22] and other fields. Most EITs require harsh experimental conditions, such as ultralow temperatures and strong laser irradiation. Compared with traditional

S.-y. Liao, J.-y. Sui, Q. Chen, H.-F. Zhang, B.-X. Li
College of Electronic and Optical Engineering and the College of Flexible Electronics Future Technology
Nanjing University of Posts and Telecommunications NJUPT
Nanjing 210023, P. R. China
E-mail: hanlor@njupt.edu.cn; bxli@njupt.edu.cn

The ORCID identification number(s) for the author(s) of this article can be found under https://doi.org/10.1002/andp.202300160

DOI: 10.1002/andp.202300160

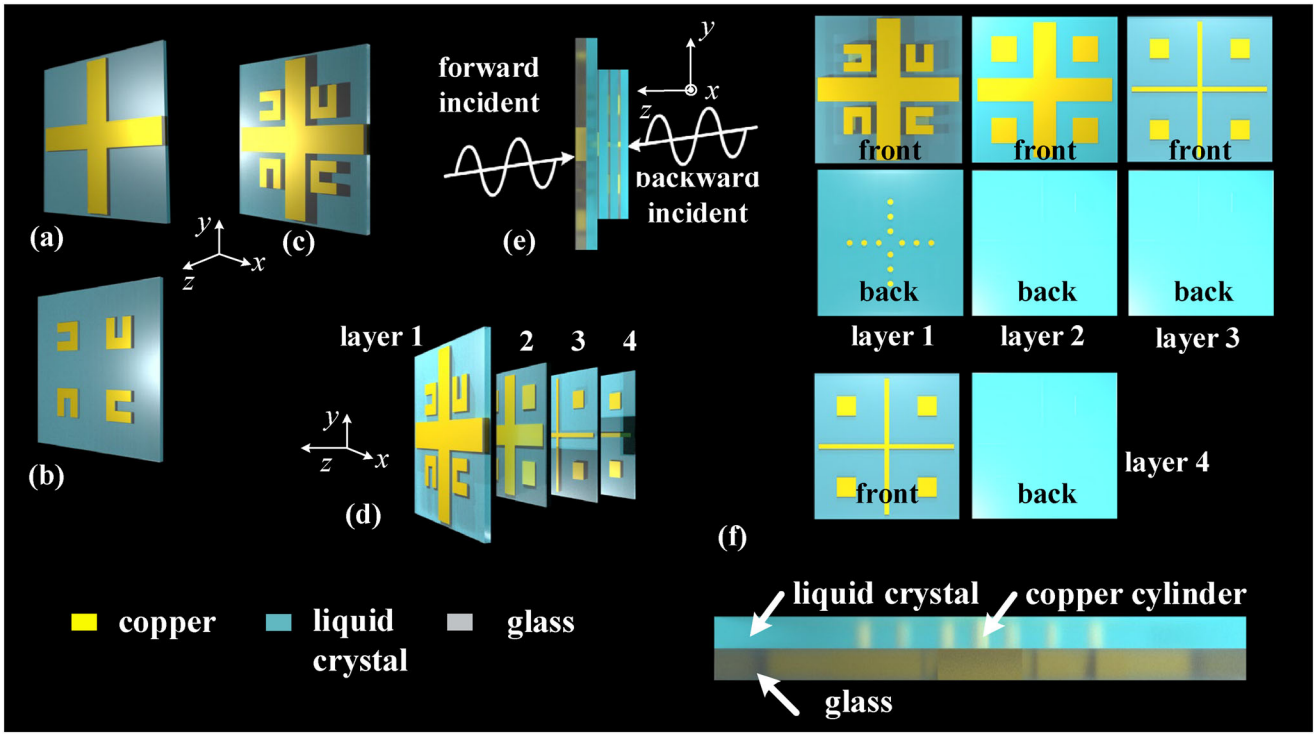

Figure 1. Perspective view of the structure, a) cross structure, b) four resonant rings, c) single-layer structure, d) four-layer structure and schematic of its forward incidence, e) schematic of its backward incidence, f) The front and back views of Layers 1–4, and side view of Layer 1, with the materials of each part indicated.

materials, metastructure has the advantages of simple structure, small size, and easy implementation of external conditions in achieving EIT. The main method to achieve EIT with metastructures is mode coupling, where the structure that can be directly excited by electromagnetic waves (EMWs) is called bright mode, and the structure that cannot be directly excited but can transfer energy through near-field coupling with bright mode is called dark mode. Classical coupling methods include bright-dark mode coupling and bright-bright mode coupling.[23–26]

NA also has many applications in the fields of sensing and detection. If the external environment can affect the frequency of the absorption peak, the external environment can be determined from the absorption peak. Commonly detected physical quantities include dielectric constant,[27] voltage,[28] refractive index,[29] etc.

According to the existing research results, due to the trend of integration, multifunctional devices are getting more and more attention. Therefore, this paper proposes a liquid crystal-based JMD, which achieves Janus properties through large-angle incidence, and realizes bidirectional EIT at an incident angle of 50°, while also incorporating backward NA characteristics, with the working frequency band controlled by the liquid crystal. The specific performance is: when EMW is incident, the transmission at 0.46–0.51 THz and 0.51–0.575 THz is achieved depending on the direction of the liquid crystal optical axis, with a group delay (GD) of 2.75 ps. When EMW is incident backward, the absorption peaks are located at either 0.331 or 0.305 THz, with absorption rates of 84.1% and 93.3%, respectively. This JMD combines EIT and NA to provide an idea for combining sensing and frequency selection functions, which can be used in the fields of communication, frequency selection, slow light, and other areas.

2. Theory and Design

2.1. Theoretical Analysis

As shown in **Figure 1**, the JMD has a four-layer stacked structure, with similar topology between each layer, but there are scaling differences in size and some details. The single-layer structure can be divided into two parts, namely, the cross structure shown in Figure 1a and the resonant rings shown in Figure 1b. These two structures are coupled to each other to form the EIT. As shown in Figure 1c, the single-layer pattern consists of resonant rings and crosses, and glass in the same layer is used to encapsulate and separate different layers of liquid crystals, as indicated in blue in the figure.

Figure 1d,e show the hierarchical structure of the final JMD and the direction of wave incidence, with a distance between layers to facilitate understanding. In addition, for ease of description, the four layers from top to bottom are named Layer 1–4 along the *z*-axis. It can be observed that the size of Layers 1–4 gradually decreases, but the overall patterns remain the same, with the only difference being that the four resonant rings are replaced with four squares. It should be noted that a set of copper cylinders is embedded in the liquid crystal between Layers 1 and 2 so that the crosses of Layers 1 and 2 are connected in the final device. The effect of this operation is to suppress interlayer resonances not mediated by liquid crystals.

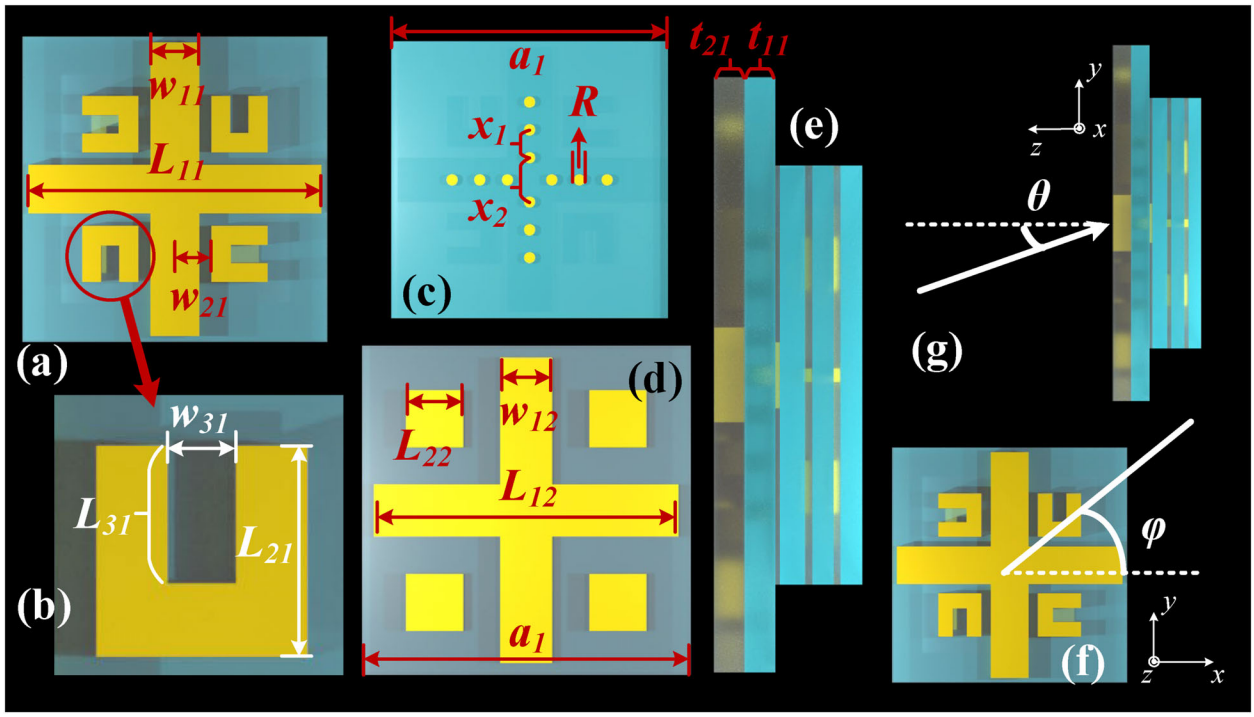

Figure 2. Parameter diagram of a) pattern of Layer 1, b) resonance ring, c) copper cylinder in Layer 1, d) pattern of Layer 2, e) thickness of different layers, and definition of g) incident angle θ, f) polarization angle φ.

On the other hand, for the resonant rings in Layer 1 and the squares in Layers 2–3, their centers coincide on the x–y plane, which means that the upper layer can effectively block the lower layers.

The definitions of the EMW incident direction and single-layer size parameters during the work are presented in **Figure 2**. Hereafter, unless otherwise specified, all data are obtained under the conditions of the incident angle θ=50° and the incident wave polarized along the y direction. Parameters of the Layer 1 top view are shown in Figure 2a,b, while the embedding positions of the Layer 1 backside cylinder are given in Figure 2c. The top view and related parameters of Layer 2–4 are displayed in Figure 2d. The side view of the four-layer structure is illustrated in Figure 2e, and only the thickness of the first layer is labeled for brevity. The relevant parameters of the remaining layers are expressed in the subsequent text. As an example, the subscript of parameter L_{21} denotes the parameter L_2 in Layer 1, and the parameters L_{22} and L_{23} in Layers 2 and 3 are expressed as L_2 parameters. It should be noted that Layer 4 parameters are not given separately since they have the same size as Layer 3. Figure 2f,g indicate the definitions of θ and φ, respectively.

The material parameters are selected as follows: the dielectric constant of the glass is ϵ_g=4,[30] and the electrical conductivity of copper is σ=5.8×10^7 S m^{-1}.[31] As the selected liquid crystal is a uniaxial crystal, its dielectric constant is expressed as follows:

$$\boldsymbol{\epsilon} = \begin{bmatrix} \epsilon_{\perp} & 0 & 0 \\ 0 & \epsilon_{//} & 0 \\ 0 & 0 & \epsilon_{//} \end{bmatrix} \quad \boldsymbol{\epsilon}_{\mathrm{E}} = \begin{bmatrix} \epsilon_{//} & 0 & 0 \\ 0 & \epsilon_{\perp} & 0 \\ 0 & 0 & \epsilon_{//} \end{bmatrix} \tag{1}$$

$$\epsilon_{eff} = \left(\frac{\cos^2\beta}{\epsilon_{\perp}} + \frac{\sin^2\beta}{\epsilon_{//}} \right)^{-1} \tag{2}$$

where $\epsilon_{//}$ represents the dielectric constant in the direction of the optical axis, and $\epsilon_{\perp}$ represents the dielectric constant perpendicular to the optical axis. The orientation of the axis can be controlled by an external electric field, as shown in **Figure 3**. When no electric field is applied, the long axis of the liquid crystal is along the horizontal direction, i.e., the matrix indicated by $\boldsymbol{\epsilon}$. And when an electric field is applied externally, the long axis of the liquid crystal is gradually deflected with the enhancement of the electric field until the fully biased state, as shown in the lower part of Figure 3. When the liquid crystal is deflected to the intermediate state, the equivalent dielectric constant is used to express the electromagnetic properties of the material, as in Equation (2), where β represents the deflection angle. The dielectric constant in the fully biased state is represented by the matrix $\boldsymbol{\epsilon}_{\mathrm{E}}$. The value of the voltage at a fully biased state varies with the liquid crystal model, boundary conditions, etc. These effects are not considered in this paper, and only the orientation of the liquid crystal optical axis is used to characterize the transition between the two states. The liquid crystal constant selected for this device is $\epsilon_{\perp}$ =3.7, $\epsilon_{//}$=8.5, with reference to the liquid crystal model HNG736600-000.

In order to accurately measure the device performance, the relevant parameters of the incident wave composed of x-polarized wave and y-polarized wave are introduced:

$$\mathrm{E}_{\mathrm{ref}} = \begin{bmatrix} r_{xx} & r_{xy} \\ r_{yx} & r_{yy} \end{bmatrix} \begin{bmatrix} E_x \\ E_y \end{bmatrix} \tag{3}$$

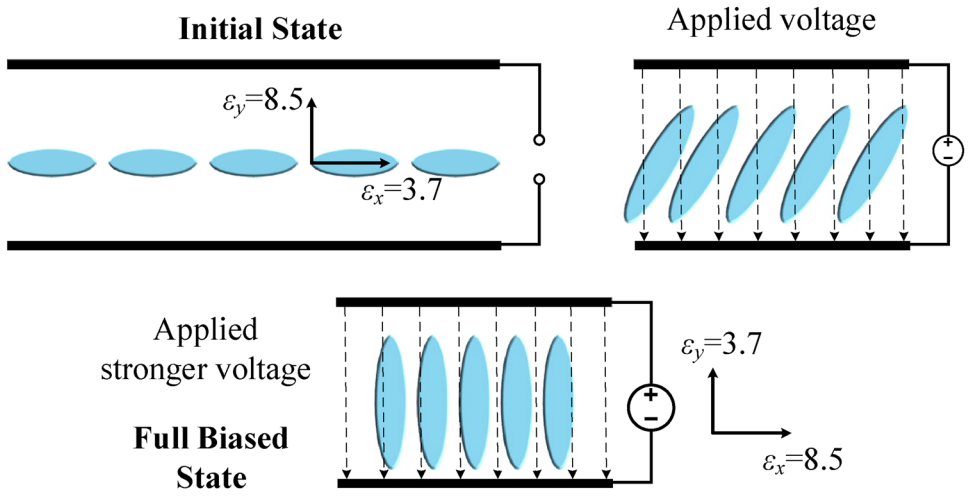

Figure 3. Schematic diagram of regulation effect of voltage on liquid crystal.

$$E_t = \begin{bmatrix} t_{xx} & t_{xy} \\ t_{yx} & t_{yy} \end{bmatrix} \begin{bmatrix} E_x \\ E_y \end{bmatrix} \tag{4}$$

$$A = 1 - R - T \tag{5}$$

In the above equation, taking the x-polarized incident EMW as an example, r_{xx} and r_{yx} represent co-polarized and cross-polarized reflection coefficients, while t_{xx} and t_{yx} represent co-polarized and cross-polarized transmission coefficients. A represents absorption, $R=r_{xx}^2+r_{yx}^2$ represents reflection, and $T=t_{xx}^2+t_{yx}^2$ represents transmission.

The EMW polarization direction can be defined as demonstrated in Figure 2f. The polarization direction along the x-axis is E_x, and along the y-axis is E_y. For the case of EMW incidence, usually only one polarization direction is considered. In the following discussion, E_x=0 and the default EMW is polarized along the y direction.

For EIT, GD is an important indicator, and the calculation method is as follows:[32]

$$\tau = \frac{\partial \Psi}{\partial \omega} \tag{6}$$

where Ψ represents the phase and ω is the angular frequency.

2.2. Single Layer Structure

All simulations in this paper were performed using HFSS and solved by the finite element method. The default background material is selected as vacuum. The xy plane is a periodic boundary, and the Z direction is selected as open space. The grid division density needs to ensure the number of grids on the longest side in each unit period is not less than 12.

For the analysis of the single-layer structure, the calculations were performed using the dimensions of Layer 1, but without the copper cylinders embedded in the liquid crystal of Layer 1, as displayed in Figure 1c. The initial direction of the liquid crystal optical axis is chosen to be along the y-axis (ϵ_x=8.5, ϵ_y=3.7), θ=50°, and the incident EWM is y-polarized (E_y). As shown in **Figure 4**, a single cross structure exhibited a transmission zero at 0.335 THz, and the square structure showed a transmission minimum at 0.625 THz. When the two were coupled, a transparent window is generated in the range of 0.337–0.692 THz, and the transmission rate exceeded 90% in the range of 0.537–0.612 THz, with a relative bandwidth (RB) of 13%. Figure 4d shows the curve of the GD, which indicates that the GD is ≈2.75 ps at a transmission rate >90%, leading to the emergence of EIT phenomena. From the transmission curves, it can be seen that since both structures can be excited individually, they belong to the bright-bright mode coupling. Figure 4e depicts the loss of the monolayer structure, where the monolayer structure has no absorbing capacity. The single-layer structure does not yet have Janus characteristics, and when the EMW is incident along the forward and backward directions, the transmission curve and absorption curve are the same.

2.3. Multilayer Structure

A four-layer structure was obtained by stacking single-layer structure from top to bottom and gradually reducing the size, with a copper cylinder embedded in the liquid crystal of the first layer to optimize performance, as demonstrated in Figure 1d,f. After stacking, as shown in **Figure 5**a, a transparent window is produced when the EMW is incident at a forward angle of 50°, and an absorption peak can be generated when the EMW is incident backward, as illustrated in Figure 5b. When the optical axis of the liquid crystal is oriented in the y direction, the transparent window ranges from 0.356 to 0.66 THz, the transmittance exceeds 90% in the range of 0.51–0.575 THz, the RB is 11.98%, and the absorption peak reaches 93.3% at 0.305 THz. When the optical axis is oriented along the x direction, the transparent window ranges from 0.36 to 0.63 THz, the transmittance exceeds 90% in the range of 0.46–0.51 THz, the RB is 10.3%, and the absorption peak reaches 84.1% at 0.331 THz. The GD of EIT is shown in Figure 5c. In Figure 5d, a comparison of the transmissivity curves of single layer and multilayer under the same bias state is provided. Due to the multilayer stack structure, the peak

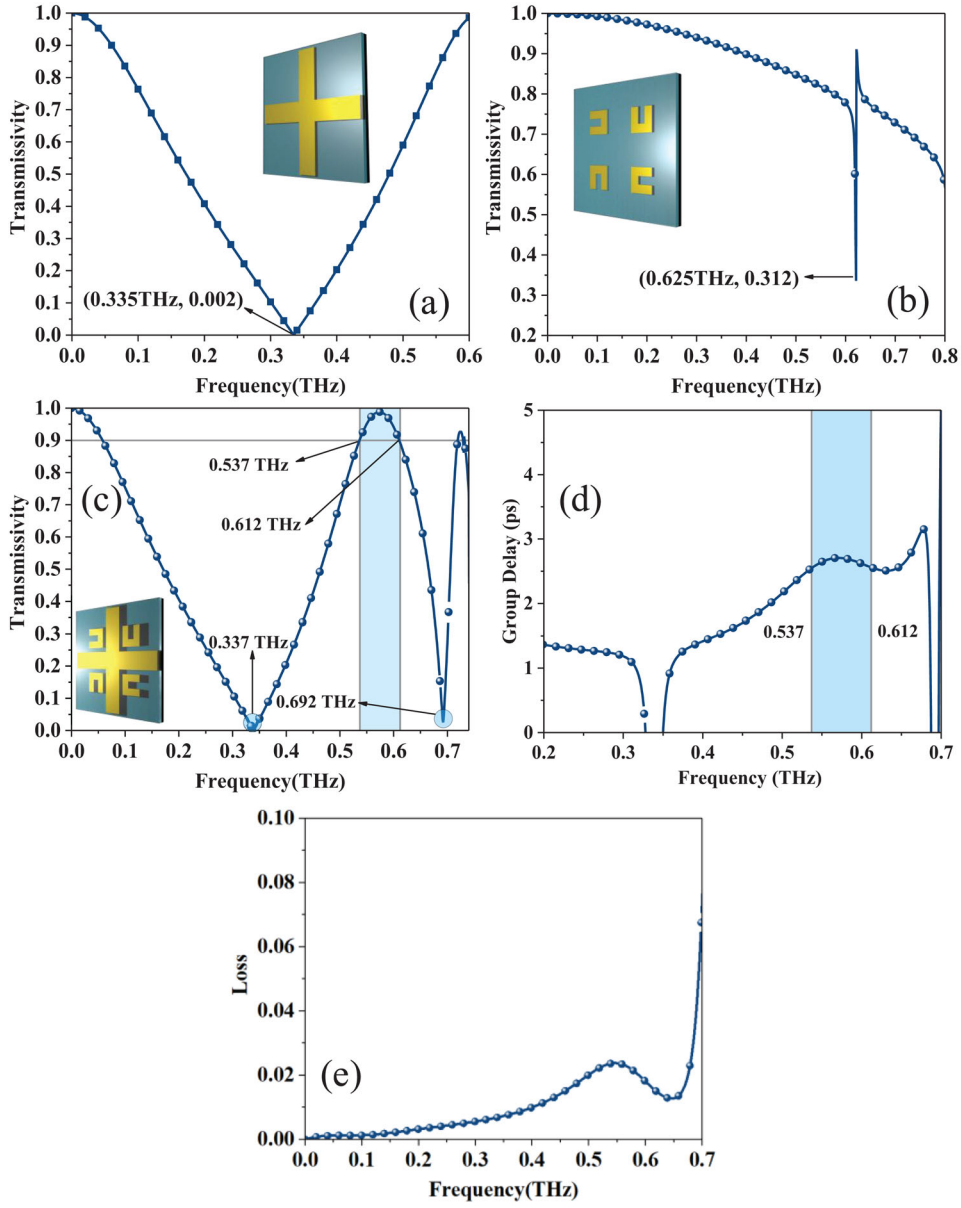

Figure 4. The transmissivity of a) cross structure, b) resonance rings, c) single layer structure. d) GD of single layer. e) Loss of single layer.

transmittance shifts to lower frequencies, the bandwidth is slightly reduced, and the overall effect is not great. This change in bandwidth is perfectly acceptable given the absorption characteristics obtained. On the other hand, considering possible polarization conversion, the reflection coefficient r_{yy} and transmission coefficient t_{yy} of co-polarization, and the reflection coefficient r_{xy} and transmission coefficient t_{xy} of cross-polarization are presented in Figure 5e,f (backward incident, ϵ_x=8.5, ϵ_y=3.7). It is easy to see that the cross-polarization coefficient can be treated as 0 for both reflection and transmission. In Figure 5e, it is evident that r_{yy} exhibits a minimum ≈0.3 THz, which corresponds to the absorption peak, and another minimum in the interval from 0.5 to 0.6 THz, which corresponds to EIT. The size parameters of JMD are shown in **Table 1**. The performance achieved by the JMD is listed in **Table 2**. The range of EIT in the table is selected as the area with transmittance >0.9, and the NA frequency is the frequency point where the absorption peak is located.

3. Results and Discussion

3.1. Mechanism Analysis

Further analysis of the energy distribution of the single-layer structure, as shown in **Figure 6**, can determine the formation conditions of the transmission valley bottoms of the two individual structures. A comparison of Figure 6 with Figure 4a,b reveals that: the transmission valley bottom of the cross-structure results from the structure being mismatched with the incident frequency, resulting in weak energy at 0.336 THz, while the transmission minimum at the resonant ring results from the

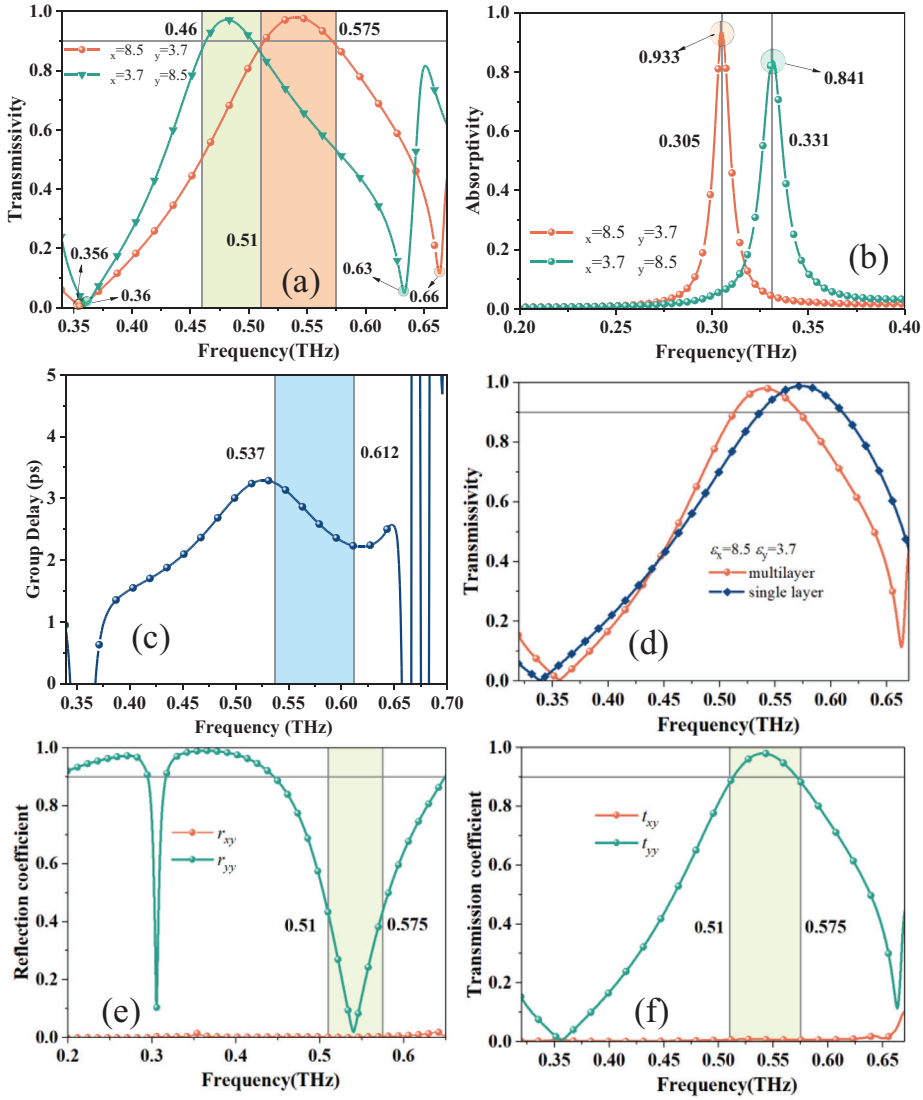

Figure 5. When θ=50° and EMW is *y*-polarized, a) EIT, b) absorption regulated by liquid crystal, c) GD of multilayer, d) comparison of transmissivity of single layer and multi-layer in the same bias state.

Table 1. Size parameters of JMD.

a_1 [μm]	a_2 [μm]	a_3 [μm]	L_{11} [μm]	L_{12} [μm]	L_{13} [μm]	L_{21} [μm]	L_{22} [μm]
250	190	190	240	180	180	46	33
L_{23} [μm]	L_{31} [μm]	R [μm]	t_{11} [μm]	t_{12} [μm]	t_{13} [μm]	t_{21} [μm]	t_{22} [μm]
25	30	10	8	7	6	8	2
t_{23} [μm]	w_{11} [μm]	w_{12} [μm]	w_{13} [μm]	w_{21} [μm]	w_{31} [μm]	x_1 [μm]	x_2 [μm]
2	40	30	6	30	15	40	25

resonance at 0.625 THz and stronger absorption leading to the minimum. The following graphs were obtained when ϵ_x=8.5 and ϵ_y=3.7. As can be seen, the transmittance minimal value at lower frequency is due to the inability of the EMWs to excite structural responses, leading to a substantial amount of reflection. This is the reason for the weaker energy observed in Figure 6a. In the higher frequency range, as shown in Figure 6b, the energy density is stronger, and consequently, the transmittance increases. A comparison between Figure 6c,d reveals the cause of the transmittance minimal value at higher frequency: at the

Table 2. Performance of JMD.

bias state incident direction	Forward	Backward
ϵ_x=8.5, ϵ_y=3.7	EIT: 0.51–0.575 THz	EIT: 0.51–0.575 THz NA: 0.305 THz
ϵ_x=3.7, ϵ_y=8.5	EIT: 0.46–0.51 THz	EIT: 0.46–0.51 THz NA: 0.331 THz

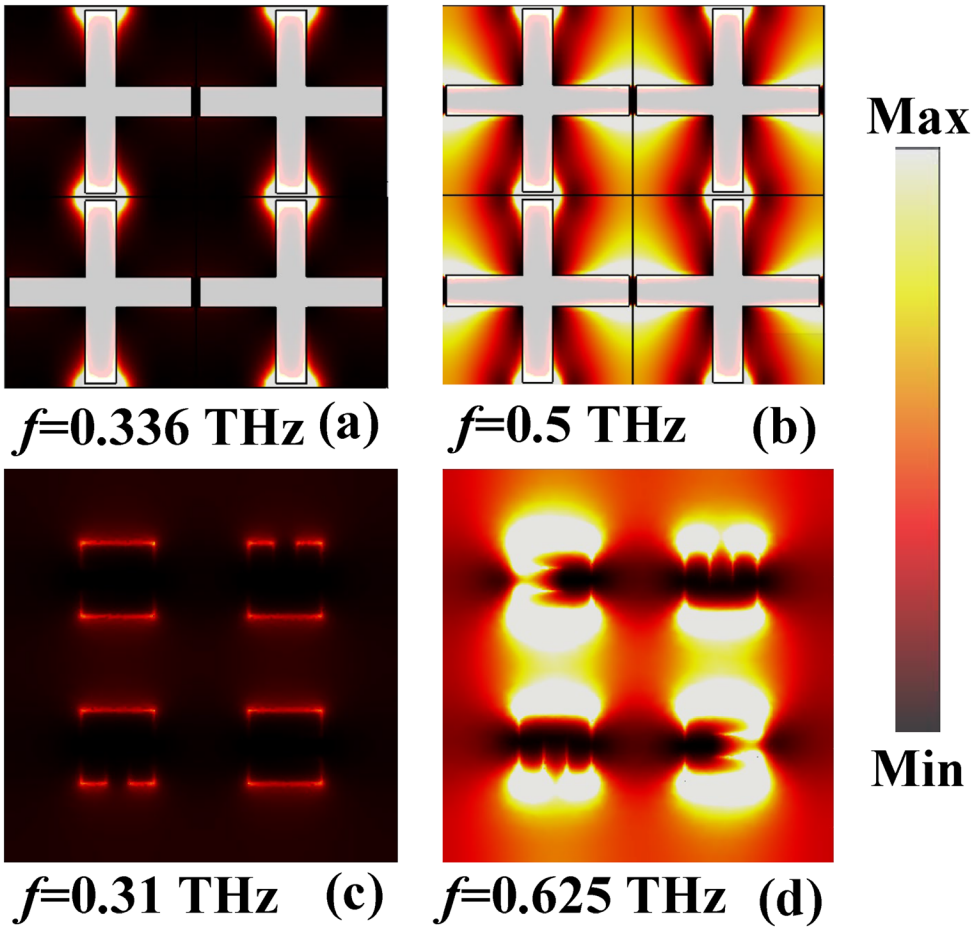

Figure 6. Energy density diagrams of cross structure a) 0.336 THz, b) 0.5 THz and resonance rings c) 0.31, d) 0.625 THz when ϵ_x=8.5 and ϵ_y=3.7.

frequency point, the resonant rings generate strong resonance, concentrating a significant amount of energy on the rings. The absorption caused by resonance is the reason for the decrease in transmittance. At lower frequencies, the energy on the resonant rings noticeably decreases, resulting in an increase in transmittance.

According to the origin of EIT, it can be explained using atomic energy level theory. In the theoretical analysis, there is no requirement for the orientation of the liquid crystal, and both bias states are permitted. In a three-level system, level |1> is the ground state, and levels |2> and |3> are excited states corresponding to the cross structure and resonant ring structure, respectively. When the EMW is incident, the coupling process between the energy and cross structure is the process of the atom being excited from |2>. When the cross structure is excited, the energy is coupled to the resonant ring structure, i.e., the transition of |3> to |2>. Under the combined effect of these two transitions, the transition path is split into two channels with similar magnitude and opposite direction, ultimately resulting in destructive interference, preventing the system from absorbing, thus leading to the formation of EIT. This process is displayed in **Figure 7**. It should be noted that the structure shown in Figure 7 is a four-layer structure. Due to the size relationship between the front and back, the back layer is completely blocked by the first layer, and only the first layer can be seen.

By analyzing the energy distribution diagram of the back incident, it can be found that the generation of the absorption peak mainly depends on the interlayer resonance. As displayed

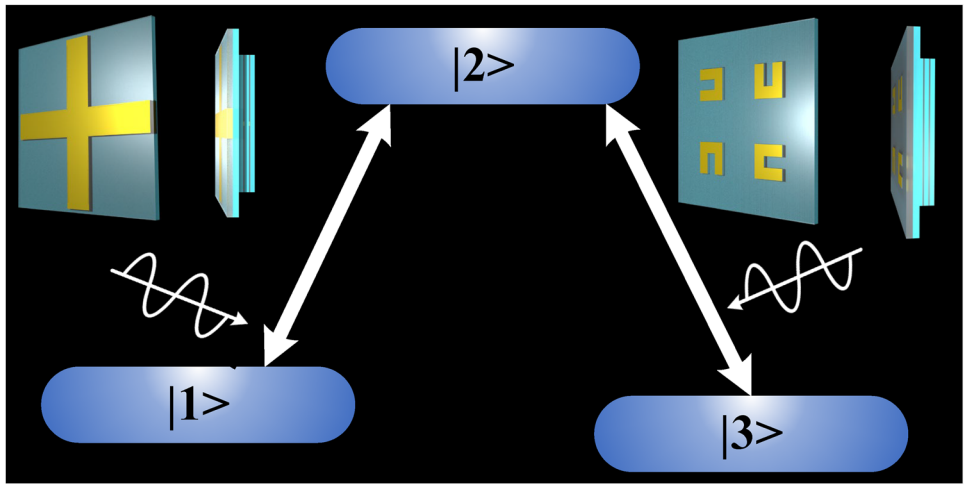

Figure 7. Atomic energy Level Explanation of JMD.

in **Figure 8b**, the energy at the absorption frequency is mainly concentrated in Layers 2–4.

During JMD's design process, a set of cylinders was embedded in the liquid crystal on Layer 1. The purpose of this is to suppress resonances that are not controlled by the liquid crystal. **Figure 9**a,b show the difference with and without cylinders. Comparing Figure 9c,d, it can be found that after adding the cylinder, the energy between Layers 1 and 2 at 0.3 THz is obviously weakened, while the energy between the next few layers remains unchanged. This energy diagram is obtained with the optical axis of the liquid crystal oriented in the *y* direction. Figure 9e,f compare the absorption curves before and after adding the cylinders. The only difference between the two is that without the addition of the cylinder there is an additional absorption peak at 0.3 THz.

As shown in **Figure 10**, when the cross structure between Layer 1 and Layer 2 is not connected, there will be an absorption peak at 0.3 THz that is not controlled by the liquid crystal axis. This will affect the use of the JMD NA characteristics. When the optical axis is oriented in the *x*-direction, the two absorption peaks are separated. By separately observing the energy distribution, it can be found that the uncontrolled absorption at 0.3 THz is generated from the resonance between Layers 1 and 2. This conclusion corroborates with the results in Figure 9, again proving that the copper cylinders in Layer 1 can eliminate the absorption peaks caused by the unmodulated interlayer resonance of liquid crystals.

3.2. Parameters Discussion

The following data is obtained with the optical axis of the liquid crystal oriented in the *y*-direction (ϵ_x=8.5, ϵ_y=3.7).

Due to the large number of parameters involved in the design process, only a few parameters that have a significant impact on performance are listed, including parameters that affect EIT: periodic length a, and parameters that affect NA: periodic length a_2 and width of cross-structure w_{13}.

Performance curves are given with the optical axis in the *y* direction. **Figure 11** shows the impact of these parameters on

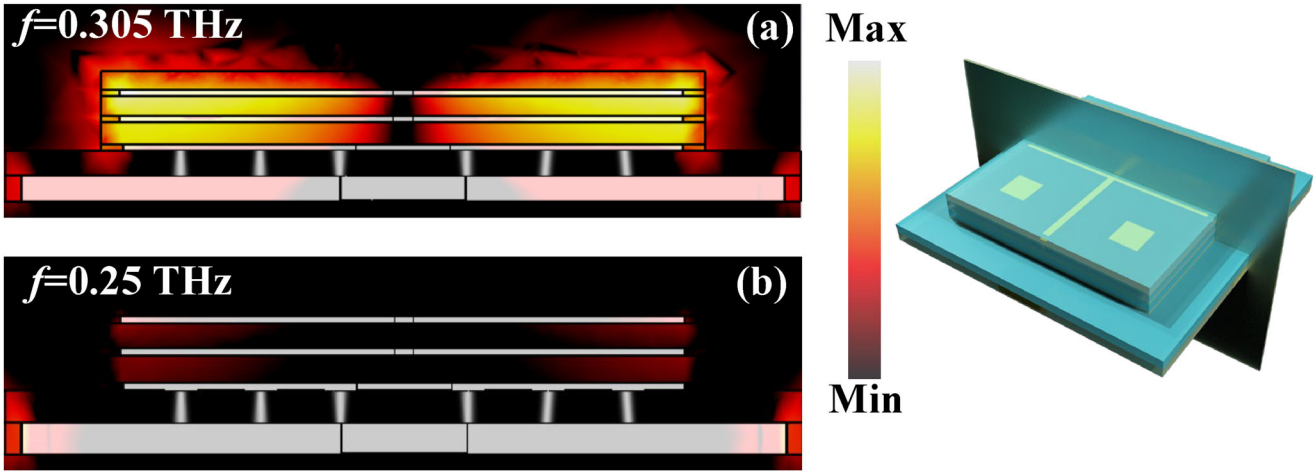

Figure 8. Energy density diagram at a) 0.305 THz, b) 0.25 THz when θ=50°, ϵ_x=8.5 and ϵ_y=3.7.

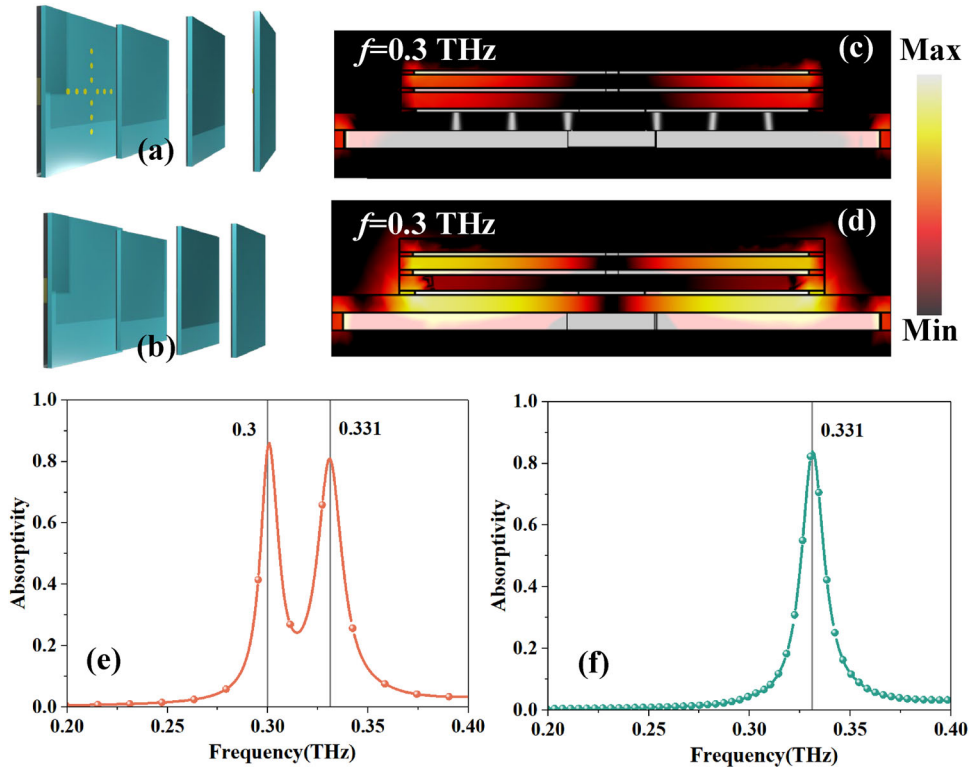

Figure 9. Structure, energy density diagram and absorption a) with copper cylinder, c) at 0.3 THz, e) absorption curve, and b) without copper cylinder, d) at 0.3 THz, f) absorption curve, when θ=50°, ϵ_x=8.5 and ϵ_y=3.7.

transmission or absorption. The transmission curve is presented in a contour plot, while the absorption peak is presented in a waterfall plot due to its narrow width. As can be seen from Figure 11a, the transparent window gradually increases as the parameter a increases, but a comparison with Figure 11b shows that when a is >250 μm, the absorption peak starts to gradually decrease. Therefore, in order to take both EIT and NA into consideration, the value of 250 μm was selected as a suitable value of a. The remaining parameters have no significant effect on the EIT transmission window within a large variation range, or the effect on the curve is not within the working band, so they will not be discussed here. Changes in a_2 affect the peak value and frequency of the absorption peak, as illustrated in Figure 11c. As a_2 reduces, the value of the absorption peak decreases, while the frequency band gradually shifts to higher frequencies. From the perspective of device use, the minimum value before the peak is significantly reduced, that is, a_2 is equal to 190 μm, so that the frequencies of EIT and NA are as close as possible. In Figure 11d, when w_{13} is changed, a slight absorption peak appears to the right of the absorption peak, which is not

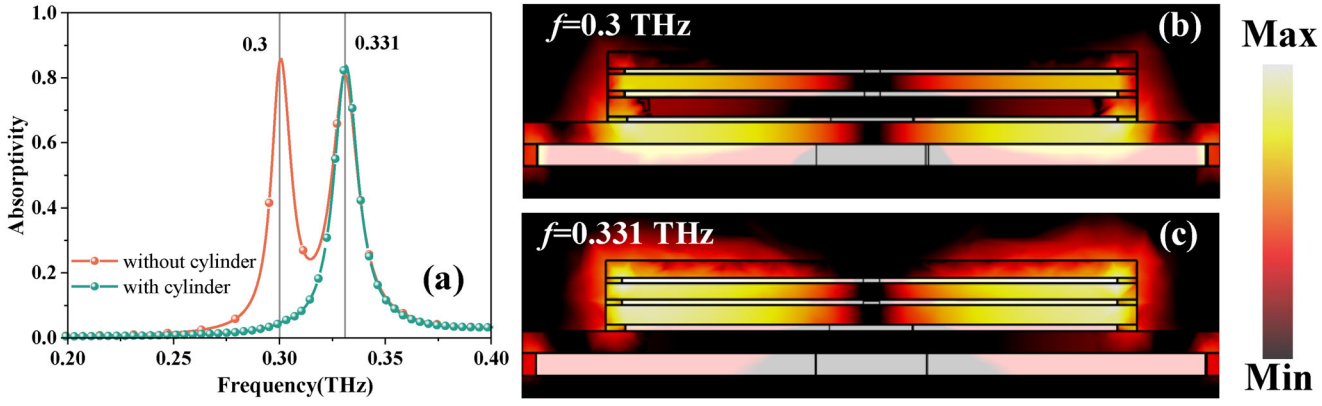

Figure 10. a) Absorptivity of structure with cylinder and without cylinder. And energy density diagram of structure without cylinder at b) 0.3, c) 0.331 THz.

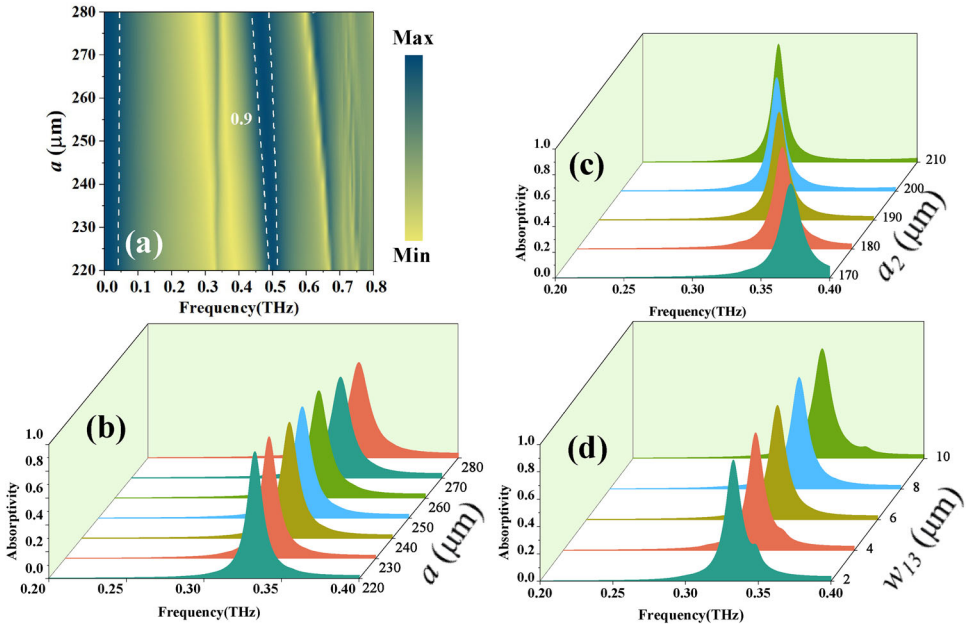

Figure 11. Parameters discussion when the optical axis of liquid crystal is along the *y*-direction (ϵ_x=8.5, ϵ_y=3.7): a) EIT with different *a*, NA with different b) *a*, c) a_2, and d) w_{12}.

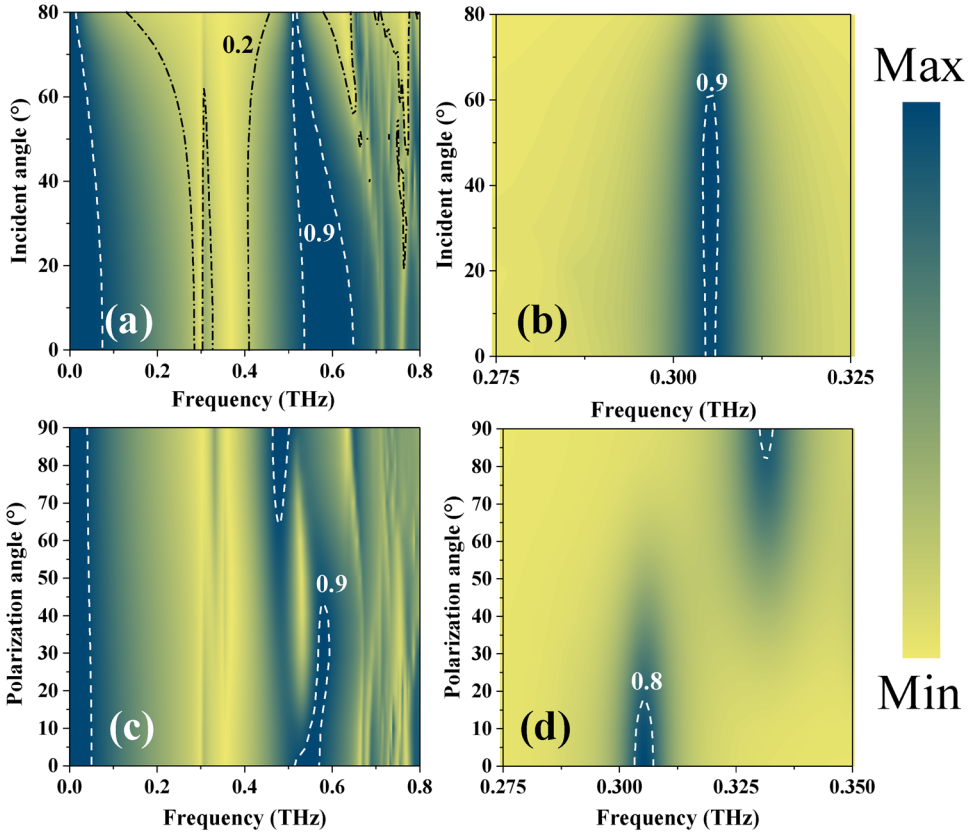

Figure 12. Transmissivity at different a) θ, c) φ and absorptivity at different b) θ, d) φ, when ϵ_x=8.5, ϵ_y=3.7.

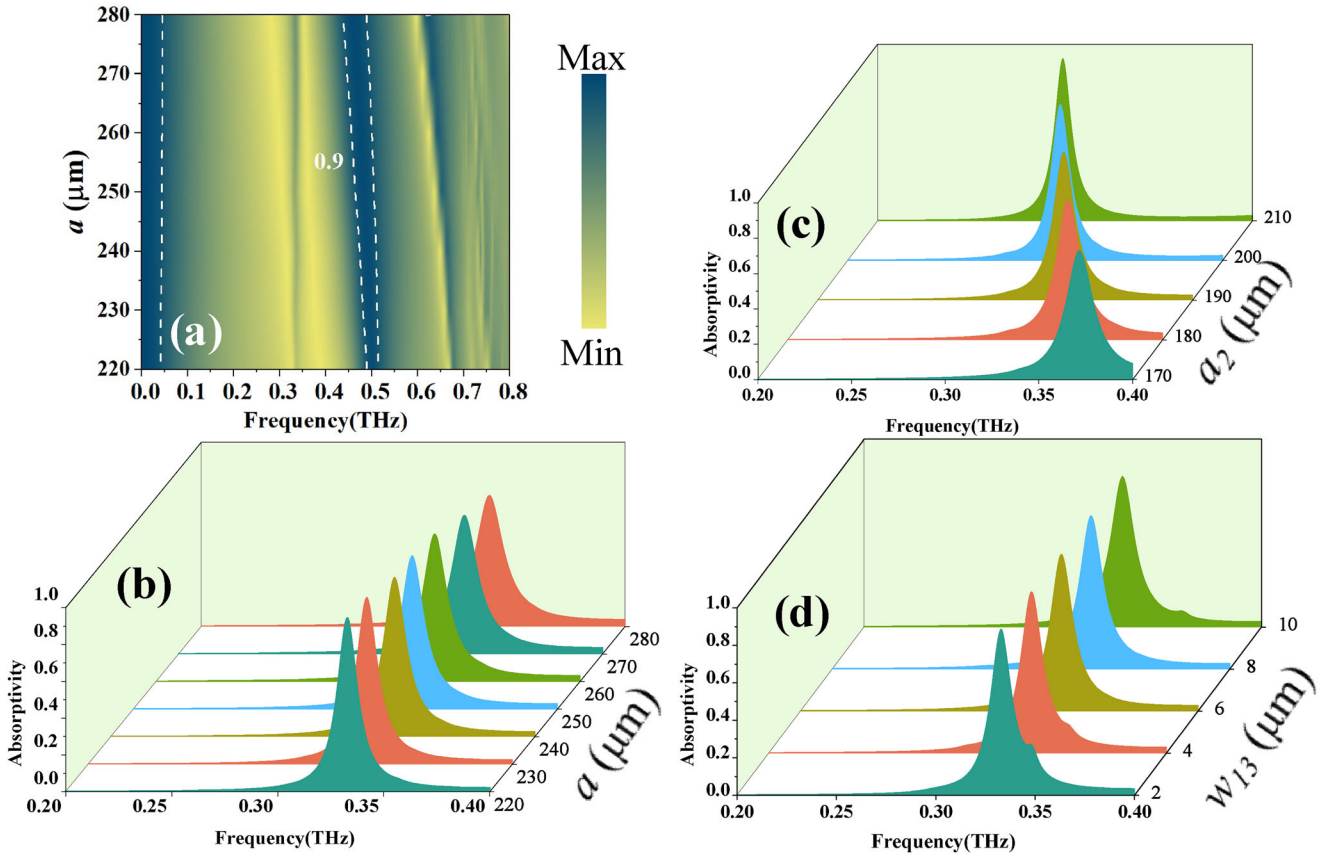

Figure 13. Parameters discussion when the optical axis is along the *x* direction: a) EIT with different *a*, NA with different b) *a*, c) a_2, d) w_{12}.

required for an ideal device. Therefore, only the interval from 6 to 8 μm is feasible and the final value was chosen to be thinner.

In addition, angle stability is also an important parameter. Since there is no essential change in the performance of liquid crystals under the two bias states, the changing trends of the performance curves are similar, and the performances discussed below are given when the optical axis is along the *y* direction. **Figure 12** shows the parameters corresponding to different θ and polar angles when θ=50°. Figure 12a,b give the EIT and NA for different incident angles. The width of the transparent window decreases with increasing θ, but the transmission zero point on the right reduces below 0.2 only for θ = 50°. On the other hand, the peak absorption decreases at an angle of incidence until it drops below 90% after θ = 60°. Taking the two into consideration, the incident angle of 50° is the most suitable. Figure 12c,d show the EIT and NA performance at different φ. Due to the anisotropic material and oblique incidence, the polarization characteristics are not symmetrical over a 90° range of variation. As φ increases, a depression appears at the center of the transmission peak, while the absorption peak drops below 0.9 after 10° and below 0.8 after 20°. It can therefore be concluded that this JMD can accept a polarization angle deviation of ≈10°.

The performance when the optical axis is along the *x* direction is as follows. F It can be seen from **Figure 13** that the variation trend of various parameters is similar to Figure 11, except that the operating frequency of EIT moves to lower frequency, while the absorption peak moves to higher frequency. In Figure 13d, the small absorption peak on the right side of the absorption peak is more obvious. In **Figure 14**a,b, the trend is also similar, except that the absorption peak value is slightly lower, which is consistent with the aforementioned simulation results. Interestingly, the spectra in Figure 14c,d are exactly opposite to those in Figure 12c,d, i.e., the 90° in Figure 14c is the same as the 0° in Figure 12c. This phenomenon is consistent with the mechanism of liquid crystal adjustment, that is, the relative position changes when the polarization angle is equal to 90°, which is the same as the optical axis of liquid crystal rotates 90° through external voltage control. Therefore, it is reasonable to obtain the same result if the polarization direction of electromagnetic waves rotated accordingly.

3.3. Parametric Inversion

By parametric inversion, the effective impedance *Z*, equivalent permeability ϵ, and equivalent permittivity μ of the device can be obtained. Considering that the NA and EIT functions can be achieved simultaneously in the backward incidence, the inversion results of the parameters in the backward incidence are given.

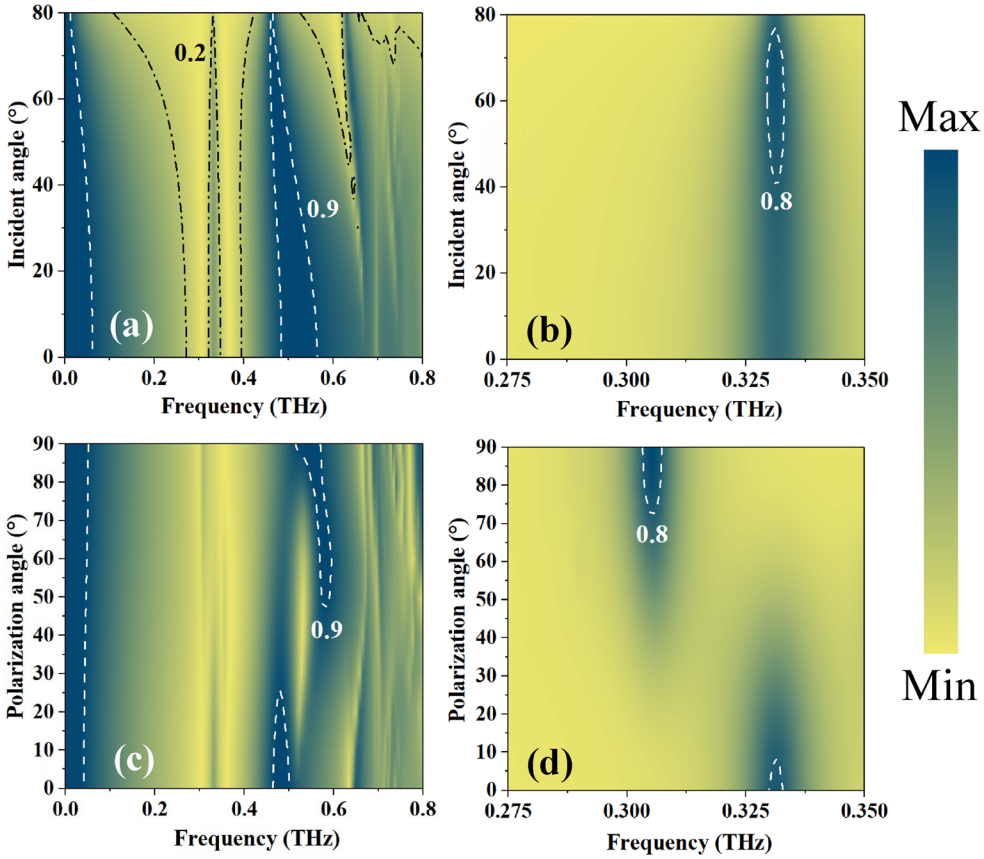

Figure 14. Transmissivity at different a) θ, c) φ and absorptivity at different b) θ, d) φ, when the optical axis is along the x direction.

For the two control states of the liquid crystal, **Figure 15**a,b show the ϵ and Figure 15c,d display the μ. Considering the device as a whole, its performance is influenced by both the ϵ and μ, therefore, both parameters need to be analyzed simultaneously. Obviously, the index Z is jointly determined by ϵ and μ, and can reflect the influence of both. In Figure 15e,f, it can be observed that Z is relatively small near the transmission band of the EIT, while as the transmittance decreases, Z rises and appears almost as a maximum near the transmission zero point. This phenomenon indicates that the larger Z is, the lower the transmittance is, which is consistent with the existing theory. Therefore, from the point of view of equivalent impedance, the generation of EIT is related to impedance matching. However, it is worth noting that although the Z value of the circled part in the figures is not large, strong absorption or transmission occurs. This is because, in the ideal absorption state, both transmission and reflection are 0. Substituting the values into the formula for Z shows that the real part of Z is 1 and the imaginary part is 0. Therefore, Z at the absorption peak position is too close to this requirement, resulting in strong absorption rather than transmission. Comparing this result with the values within the passband range, it is not difficult to find that the values within this range also meet the requirements for strong absorption, but what appears is the transmission. This confirms the mechanism of EIT from another aspect. As mentioned earlier, it is destructive interference caused by resonance between different modes, rather than simple impedance matching causing transmission.

4. Conclusion

A liquid crystal-controlled JMD with large incidence angle, which achieves both bidirectional EIT and backward NA is proposed in this paper. When the liquid crystal optical axis is oriented in different directions, the EIT ranges with transmission rate over 90% are 0.46–0.51 THz and 0.51–0.575 THz, respectively, and the absorption peaks of NA are located at 0.305 and 0.331 THz, with peaks of 93.3% and 84.1%, respectively. In addition to this, a parametric discussion is carried out to explore the performance at different θ and φ, and a parametric inversion is carried out at the end to analyze the dielectric constant, permeability, and impedance of JMD from a theoretical perspective. Furthermore, the stacking structure is combined with Janus functionality and liquid crystal control is considered innovative. The proposed JMD can be applied in fields such as communication and signal modulation. Specifically, the properties of EIT are expected to be applied to the design of slow optical devices or electromagnetic filters. And the backward absorption properties are expected to be used in the design of detection devices, or shielding for specific frequencies. In addition, it is also possible to combine this technology with quasi-BIC[33–35] for functions such as optical field modulation.

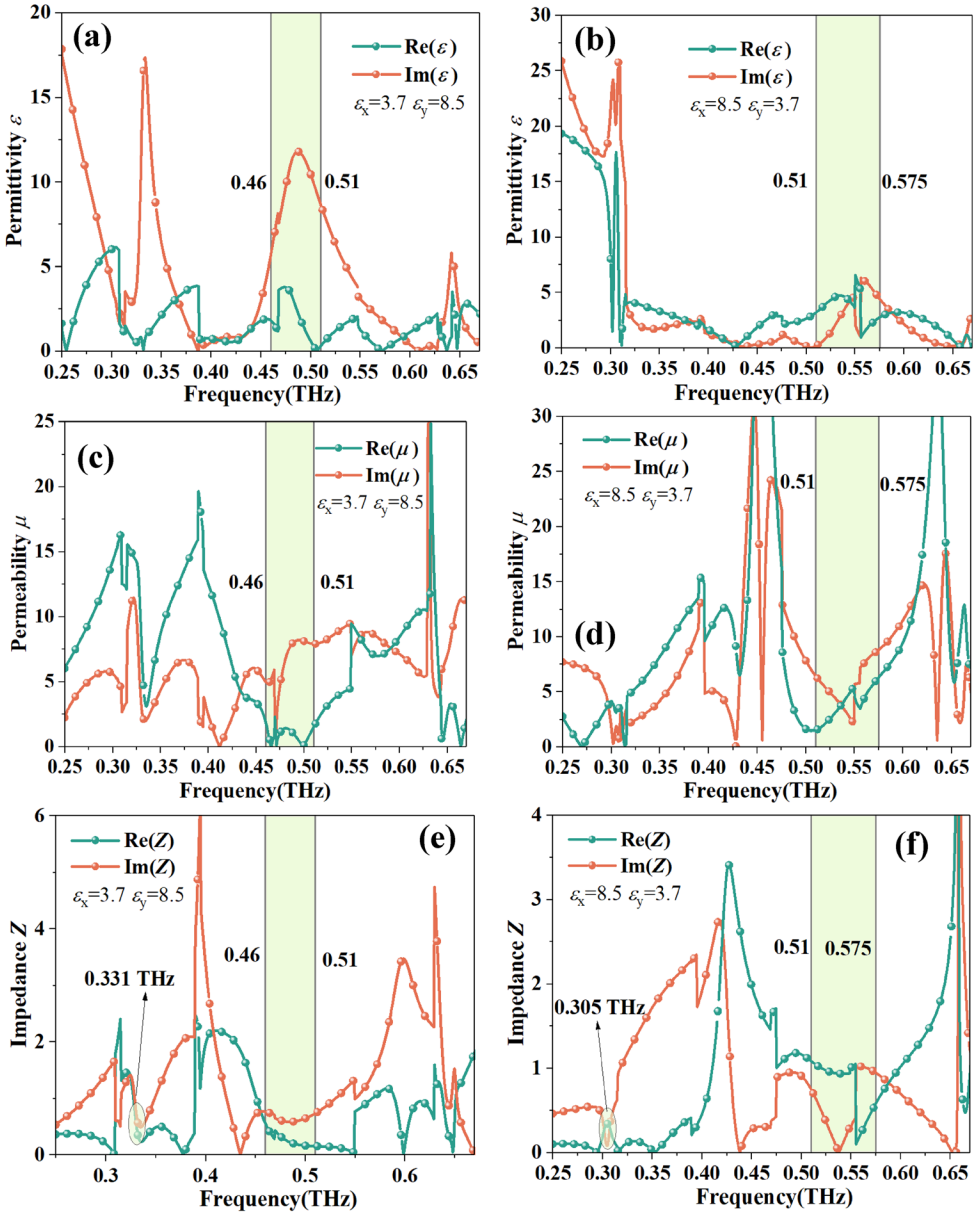

Figure 15. When EMW is incident along the backward direction and the liquid crystal optical axis is pointing in the *x*-direction (ϵ_x=3.7, ϵ_y=8.5), a) ϵ, c) μ, e) *Z*, and b) ϵ, d) μ, f) *Z* when the optical axis is in the *y*-direction (ϵ_x=8.5, ϵ_y=3.7).

Acknowledgements

This work was supported by the National Key Research and Development Program of China (Grant No.2022YFA1405000), the Natural Science Foundation of Jiangsu Province, Major Project (Grant No.BK20212004), and Natural Science Research Start-up Foundation of Recruiting Talents of Nanjing University of Posts and Telecommunications (Grant No. NY222105).

Data Availability Statement

The data that support the findings of this study are available from the corresponding author upon reasonable request.

Keywords

electromagnetic induced transparency, liquid crystal, metastructure, multifunctional device

Conflict of Interest

The authors declare no conflict of interest.

Received: April 11, 2023
Revised: July 22, 2023
Published online:

[1] Z. Xu, Y. Wang, S. Liu, J. Ma, S. Fang, H. Wu, *IEEE Sens. J.* **2023**, *23*, 6378.
[2] Y. Hu, X. Zhou, Q. Sun, G. Zeng, Y. Xiong, *IEEE Sens. J.* **2023**, *23*, 3431.
[3] W. Li, Z. Qu, J. Duan, J. Wang, J. Kang, B. Yao, B. Zhang, *Optik* **2023**, *272*, 170343.
[4] Y. Zhang, B. Jing, S. Liu, X. Hao, Z. Luo, J. Zou, S. Yin, W. Huang, W. Zhang, *Photonics MDPI.* **2023**, *10*, 159.
[5] J. Ren, T. Li, B. Fu, S. Wang, Z. Wang, S. Zhu, *Opt. Mater. Express* **2021**, *11*, 3908.
[6] J. F. Ruan, Z. F. Meng, R. Z. Zou, S. M. Pan, S. W. Ji, *Microw. Opt. Technol. Lett.* **2023**, *65*, 20.
[7] Y. Su, Y. Li, T. Yang, T. Han, Y. Sun, J. Xiong, L. Wu, C. W. Qiu, *Adv. Mater.* **2021**, *33*, 2003084.
[8] Y. Du, W. Wei, X. Zhang, Y. Li, *J. Phys. Chem.* **2018**, *122*, 7997.
[9] R. Zhang, C. Liu, N. Li, L. Chen, T. Xu, Y. Qin, S. Zhang, Z. Wang, *Ind. Eng. Chem. Res.* **2020**, *59*, 18520.
[10] M. F. Picardi, A. V. Zayats, F. J. Rodríguez-Fortuño, *Phys. Rev. Lett.* **2018**, *120*, 117402.
[11] M. F. Picardi, C. P. T. McPolin, J. J. Kingsley-Smith, X. Zhang, S. Xiao, F. J. Rodríguez-Fortuño, A. V. Zayats, *Appl. Phys. Rev.* **2022**, *9*, 021410.
[12] M. Farhat, W. W. Ahmad, A. Khelif, K. N. Salama1, Y. Wu, *J. Appl. Phys.* **2021**, *129*, 104902.
[13] T. Li, J. J. Kingsley-Smith, Y. Hu, X. Xu, S. Yan, S. Wang, B. Yao, Z. Wang, S. Zhu, *Opt. Lett.* **2023**, *48*, 255.
[14] L. Wang, Q. Fu, F. Wen, X. Zhou, X. Ding, Y. Wang, *Materials.* **2023**, *16*, 846.
[15] H. Jeong, Y. Cui, M. M. Tentzeris, S. Lim, *Addit. Manuf.* **2020**, *35*, 101405.
[16] L. Jiang, Q. Yuan, H. Yang, Y. Li, L. Zheng, Z. Zhu, S. Liang, Y. Pang, H. Wang, J. Wang, S. Qu, *Photonics Res.* **2023**, *11*, 373.
[17] R. Ning, F. Wang, W. Huang, Z. Jiao, *J. Opt.* **2022**, *1*, 7.
[18] K. J. Boller, A. Imamoğlu, S. E. Harris, *Phys. Rev. Lett.* **1991**, *66*, 2593.
[19] J. P. Marangos, *J. Mod. Opt.* **1998**, *45*, 471.
[20] G. Tai, B. Ni, X. Zhou, H. Ni, L. Yang, G. Hua, L. Huang, J. Wang, J. Chang, *Opt. Quantum Electron.* **2023**, *55*, 317.
[21] C. Li, Y. Teng, Y. Xiao, R. Su, M. Yu, Y. Juan, M. Hua, J. He, L. Jiang, *Appl. Opt.* **2022**, *61*, 9398.
[22] Y. Li, Y. Xu, J. Jiang, S. Cheng, Z. Yi, G. Xia, X. Zhou, Z. Wang, Z. Chen, *Phys. Chem. Chem. Phys.* **2023**, *25*, 3820.
[23] F. Zhang, X. He, X. Zhou, Y. Zhou, S. An, G. Yu, L. Pang, *Appl. Phys. Lett.* **2013**, *103*, 221904.
[24] L. Zhu, L. Dong, J. Guo, F. Y. Meng, X. J. He, C. H. Zhao, Q. Wu, *RSC Adv.* **2017**, *7*, 55897.
[25] Z. Wei, X. Li, N. Zhong, X. Tan, X. Zhang, H. Liu, H. Meng, R. Liang, *Plasmonics.* **2017**, *12*, 641.
[26] F. Bagci, B. Akaoglu, *J. Appl. Phys.* **2018**, *123*, 173101.
[27] M. Bakır, M. Karaaslan, E. Unal, O. Akgol, C. Sabah, *Opto-Electron. Rev.* **2017**, *25*, 318.
[28] M. Bakır, M. Karaaslan, F. Dincer, K. Delihacioglu, C. Sabah, *J Mater Sci* **2016**, *27*, 12091.
[29] B. X. Wang, G. Z. Wang, T. Sang, *J. Phys. D* **2016**, *49*, 165307.
[30] L. Zeng, H. F. Zhang, G. B. Liu, T. Huang, *Plasmonics.* **2019**, *14*, 1347.
[31] A. S. Dhillon, D. Mittal, E. Sidhu, *Optik* **2017**, *144*, 634.
[32] C. J. Ma, Y. B. Zhang, Y. Zhang, S. Q. Bao, J. S. Jin, M. Li, D. M. Li, Y. G. Liu, Y. P. Xu, *Nanoscale Adv* **2021**, *3*, 19.
[33] R. Chen, T. Li, Q. Bi, S. Wang, S. Zhu, Z. Wang, *Opt. Mater. Express* **2022**, *12*, 1232.
[34] R. Chen, Q. Bi, T. Li, S. Wang, S. Zhu, Z. Wang, *J. Opt.* **2023**, *25*, 045001.
[35] Y. Hu, M. Tong, S. Hu, W. He, X. Cheng, T. Jiang, *Adv. Funct. Mater.* **2022**, *32*, 2203680.